JGR Solid Earth

RESEARCH ARTICLE

Key Points:

- The upper mantle beneath the Changbaishan volcano is characterized by two seismic low-velocity anomalies
- The shallow low-velocity anomaly (i.e., shallow than 370 km, with a higher Vp/Vs ratio) is due to partial melting
- The deep anomaly (i.e., atop the 410-km, with a lower Vp/Vs ratio) is likely caused by the moduli reduction during the phase transformation

Supporting Information:

Supporting Information may be found in the online version of this article.

Correspondence to:

J. Li,
jli@epss.ucla.edu

Deep Geophysical Anomalies Beneath the Changbaishan Volcano

Shaohua Li[1,2] [ID], **Jiaqi Li**[3] [ID], **Thomas P. Ferrand**[4] [ID], **Tong Zhou**[5], **Mingda Lv**[6] [ID], **Ziyi Xi**[7] [ID], **Ross Maguire**[8] [ID], **Guangjie Han**[9,10,11], **Juan Li**[10,11,12] [ID], **Xiyuan Bao**[3], **Yiran Jiang**[13], and **Tiezhao Bao**[14]

[1]Gansu Lanzhou Geophysics National Observation and Research Station, Lanzhou, China, [2]Lanzhou Institute of Seismology, China Earthquake Administration, Lanzhou, China, [3]Department of Earth, Planetary, and Space Sciences, University of California Los Angeles, Los Angeles, CA, USA, [4]Institüt für Geologische Wissenschaften, Freie Universität Berlin, Berlin, Germany, [5]Aramco Research Center, Aramco Asia, Beijing, China, [6]Department of Earth and Environmental Sciences, Michigan State University, East Lansing, MI, USA, [7]Department of Computational Mathematics, Science and Engineering, Michigan State University, East Lansing, MI, USA, [8]University of Illinois at Urbana-Champaign, Champaign, IL, USA, [9]China Earthquake Networks Center, Beijing, China, [10]Key Laboratory of Earth and Planetary Physics, Institute of Geology and Geophysics, Chinese Academy of Sciences, Beijing, China, [11]College of Earth and Planetary Sciences, University of Chinese Academy of Sciences, Beijing, China, [12]Heilongjiang Mohe Observatory of Geophysics, Institute of Geology and Geophysics, Chinese Academy of Science, Beijing, China, [13]School of Earth and Space Sciences, Peking University, Beijing, China, [14]CNOOC Research Institute, Beijing, China

Abstract Subsurface imaging is key to understanding the origin of intraplate volcanoes. The Changbaishan volcano, located about 2,000 km away from the western Pacific subduction zone, has several debated origins. To investigate this, we compared regional seismic tomography with the electrical resistivity results and obtained high-resolution 1D and quasi-2D velocity-depth profiles. We show that the upper mantle is characterized by two anomalies exhibiting distinct features which cannot be explained by the same mechanism. We document a localized low-velocity anomaly atop the 410-km discontinuity, where the P-wave velocity is reduced more than that of the S-wave (i.e., lower Vp/Vs). We propose that this anomaly is caused by the reduction of the effective moduli during the phase transformation of olivine. The other anomaly, located between 300 and 370 km depth, reveals a significant reduction of the S-wave velocity (i.e., higher Vp/Vs), associated with a reduction of the electrical resistivity, altogether consistent with partial melting.

Plain Language Summary On Earth, most magmatic activities occur at plate boundaries, which can be explained by plate tectonics. However, the largest intraplate volcanic region in northeast Asia, the Changbaishan volcano, is situated on the border between North Korea and China about 2,000 km from the plate boundary and has several debated origins. We show that beneath the Changbaishan volcano, the upper mantle is characterized by two seismic velocity anomalies exhibiting distinct features which cannot be explained by the same mechanism. The shallower anomaly located between 300 and 370 km depth is interpreted to be due to a small amount of melt because of its seismic and electrical resistivity characteristics. The other deeper anomaly atop the mantle transition zone at ~ 410 km depth cannot be explained by partial melting alone and is likely caused by a change in seismic characteristics as a result of the olivine phase transition that occurs at that depth.

1. Introduction

The Changbaishan volcano is the largest intraplate volcanic region in northeast Asia and is located more than 2,000 km from the trench of the western Pacific subduction zone (Figure 1a). Due to its large distance from the convergent boundary, the origin of the magmatism cannot be simply explained by plate tectonics (Tang et al., 2014). One early study by Tatsumi et al. (1990) proposed that asthenosphere upwelling, associated with the opening of the Japan Sea, would explain the formation of the Changbaishan volcano, but its origin has continued to be debated. With the development of seismic tomography, that is, a technique to provide 2-D or 3-D seismic images of the deep Earth, structures down to the mantle transition zone provide new clues for the origin of intraplate volcanism.

Using P-wave travel times, Huang and Zhao (2006) and Chen and Pei (2010) observed a flat Pacific slab in the mantle transition zone that extend westwards up to 2,000 km from the trench. Accordingly, Zhao et al. (2009) and

Validation: Jiaqi Li, Thomas P. Ferrand, Tong Zhou, Mingda Lv, Ross Maguire, Guangjie Han, Juan Li, Xiyuan Bao
Visualization: Jiaqi Li, Thomas P. Ferrand, Ziyi Xi
Writing – original draft: Shaohua Li, Jiaqi Li
Writing – review & editing: Shaohua Li, Thomas P. Ferrand, Tong Zhou, Mingda Lv, Ziyi Xi, Ross Maguire, Guangjie Han, Juan Li, Xiyuan Bao, Yiran Jiang, Tiezhao Bao

Kuritani et al. (2011) proposed that the origin of the Changbaishan volcano is related to the dehydration of this flat (stagnant) slab. However, the expected island-arc signatures in the erupted rocks are absent, as indicated by geochemical studies (e.g., Chen et al., 2007; Zou et al., 2008). Using the differential travel time of the P waves (or S waves), Tang et al. (2014) identified a gap in the flat slab from the seismic tomography images. They thus proposed that, via this slab gap, mantle upwellings (i.e., low-velocity anomalies possibly originated from below the 660-km discontinuity) and the subsequent decompression melting at asthenosphere depths could feed the Changbaishan volcano. Although the methods employed were effective at providing the first seismic velocity models for the area, the resolution from travel-time tomography limits the detailed resolution of deep structures.

With increasing computational power, the development of efficient 3-D waveform simulation tools (Komatitsch & Tromp, 1999), and advances in inversion theory (Tromp et al., 2005), seismic tomography studies utilizing the full-waveform information have become feasible at both regional and global scales (e.g., Bozdag et al., 2016; Chen et al., 2015; Fichtner et al., 2009; French & Romanowicz, 2014; Lei et al., 2020; Tape et al., 2009; Zhu et al., 2015). For example, the regional tomographic model FWEA18 (Tao et al., 2018), derived from a data set consisting of both body waves and surface waves, has one of the highest resolutions among the full-waveform inversion models in East Asia. Owing to the relatively high-resolution images from the FWEA18 model, it is possible to further study the detailed subsurface structures down to the mantle transition zone.

More importantly, the FWEA18 model also provides an opportunity to combine the P- and S-wave models to decipher the origin of the Changbaishan volcano. For example, either the presence of volatiles (e.g., water) or high temperature could reduce the P- and S-wave speeds, but in different ways (Tseng & Chen, 2008). Specifically, from the laboratory measurement of the polymorphs of olivine, the effect of the temperature on the P- and S-wave speeds are comparable (Jackson et al., 2000; Kern, 1982; Sinogeikin et al., 1998). On the contrary, the hydration of crystal lattices or grain boundaries will cause a reduction in S-wave speed that is twice as high as the reduction in P-wave speed (Faul et al., 1994; Toomey et al., 1998).

In the cross-section along the down-dip direction and cutting through the Changbaishan volcano, the FWEA18 model shows distinct features in the P- and S-wave models. In the P-wave model (Figure 1b) the low-velocity anomaly is mainly concentrated in the vicinity of the top of the 410-km discontinuity with a maximum amplitude of −1.5%. In contrast, at depths between 300 and 370 km, no significant low-velocity anomaly is observed (i.e., less than −1.0%). In the S-wave model, there is also a low-velocity anomaly atop the 410-km discontinuity of similar or even smaller amplitude (i.e., about −1.0% to −1.5%) as that in the P-wave model (i.e., −1.5%). However, at shallower depths (i.e., 300–370 km), there are strong wave speed reductions (i.e., −1.5%), and those anomalies are distributed over a large depth range.

If such distinct behaviors in the P- and S-wave models are true features, this will indicate the low-velocity anomaly atop the 410-km discontinuity and the other one at a shallower depth (i.e., 300–370 km) likely result from different mechanisms. However, although the FWEA18 model has the highest resolution among the full-waveform inversion models, its resolution is still limited due to the lack of short-period seismic data because of the large computational costs of 3D simulations. For example, the shortest period is 8 s for the P-wave, and the corresponding resolution is about 50–80 km (Tao et al., 2018).

To determine whether the features in the FWEA18 model are valid or correspond to artifacts due to resolution issues, we need to analyze seismic data at higher frequencies, which provide better spatial resolutions. In this study, we perform 1D and quasi-2D waveform inversions with high-frequency data (i.e., the shortest period down to 2 s) to provide a more accurate 1D velocity-depth profile as "anchor points" in the cross-section of the tomographic FWEA18 model (i.e., the average 1-D model in the dashed box in Figures 1b and 1c).

2. Data and Method

2.1. Data

We selected high-quality datasets from two earthquakes whose locations allow a study along a sub-linear seismic array, that is, the cross-section located in Figure 1a. These two events occurred at a similar epicentral distance beneath the Japan Sea, but with different focal depths (Ekström et al., 2012). The first event, 20080604, occurred on 4 June 2008, with a moment magnitude of 5.7 and a focal depth of 220 km (Han et al., 2021). This relatively large event produced both clear P- and S-wave triplications, which are recorded by dense seismic stations in
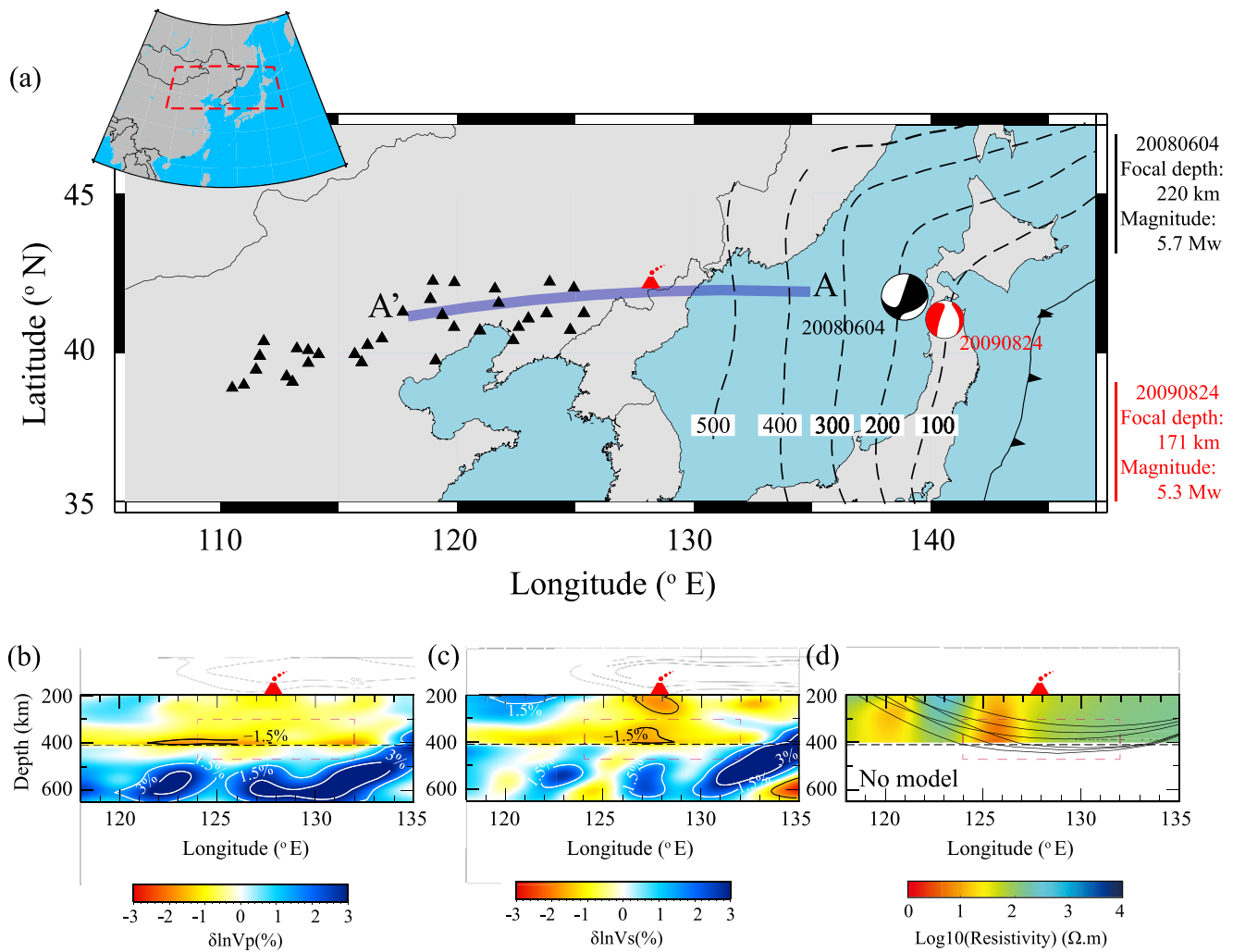
Figure 1. Research region and cross sections. (a) Research region and locations of the earthquakes (events 20080604 and 20090824 are indicated by the black and red beach balls, respectively) and the stations (the black triangles). The red triangle marks the location of the Changbaishan volcano. The dashed black lines are slab depth contours from Slab2.0 model (Hayes et al., 2018). (b) P-wave speed perturbation from FWEA18 model (Tao et al., 2018) along the cross-section AA' in (a). The red triangle denotes the location of the Changbaishan volcano. The seismic ray paths utilized in this study are shown as black curves in (d). The dashed box marks the region where the seismic data are most sensitive to. (c) Similar to (b) but for the S-wave speed perturbation. (d) Resistivity results from Li et al. (2020) approximately along the cross-section AA' in (a).

China (Figure 1a). The second event, 20090824, occurred on 24 August 2009, with a moment magnitude of 5.3 and a focal depth of 171 km. For this event, with a relatively smaller magnitude, only P-wave signals are clearly recorded.

We downloaded the continuous waveform data (300 and 1,200 s before and after the theoretical P-wave arrival) and used the Seismic Analysis Code (SAC) to remove the instrument response, with a pre-filtering from 0.01 to 8 Hz. For our triplication study, we used displacement waveforms (Figure 2) and band-pass filtered (from 0.04 to 1 Hz for the P-wave data, and 0.05–1 Hz for the S-wave data) the data with a zero-phase, second-order Butterworth filter.

2.2. Methods

2.2.1. Body Wave Triplications

Body wave triplications are sensitive to the structures near the discontinuity due to the dense ray paths of a combination of direct, reflected, and refracted waves (e.g., Bissig et al., 2022; Stähler et al., 2012; Takeuchi
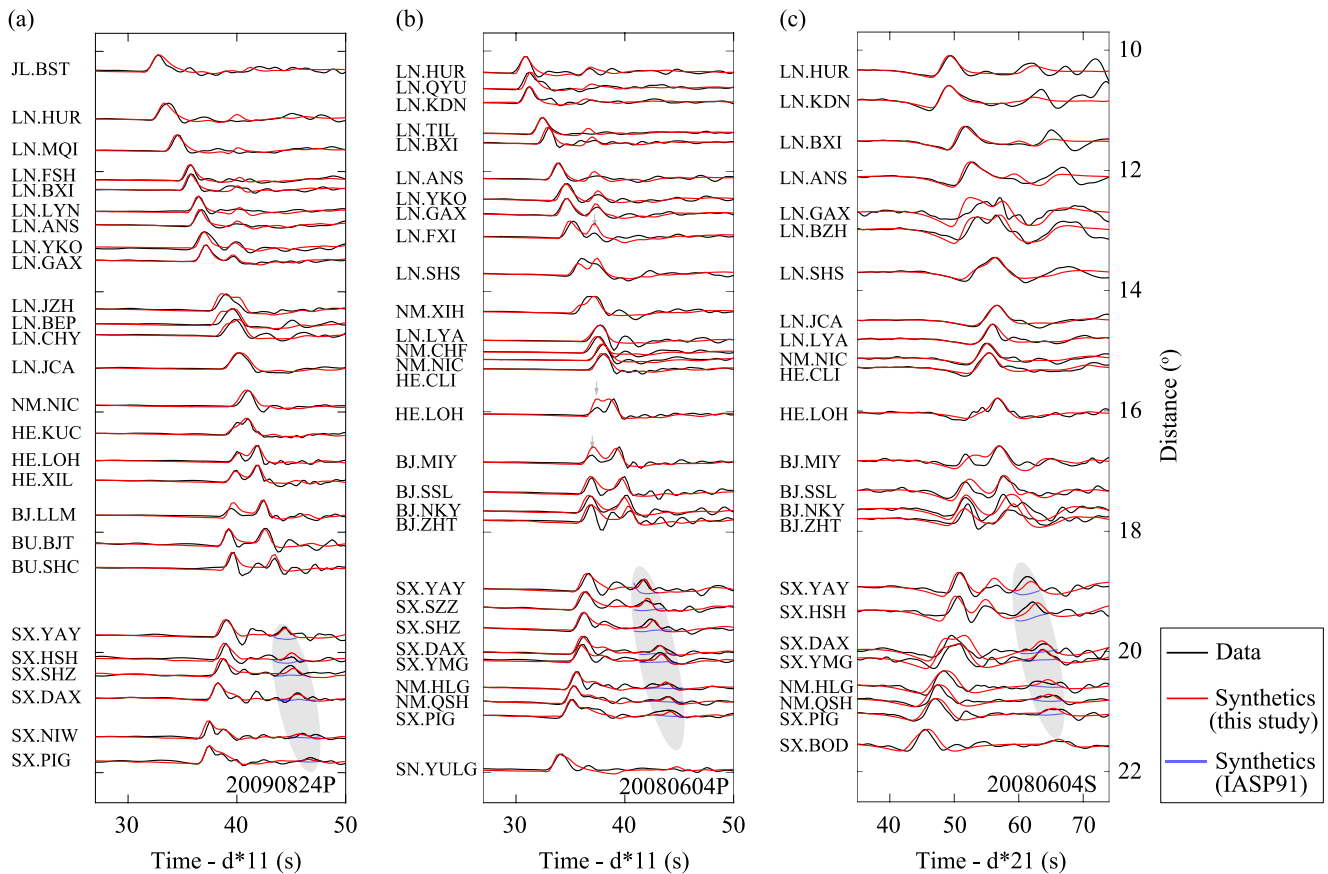
Figure 2. Seismic observations and 1D synthetic waveforms. (a) Waveform comparison between the displacement data (in black) and the synthetics (in red, calculated using the average value of the acceptable models) for the P waves of event 20090824 on the vertical component. The shaded region marks the phase which is sensitive to the low-velocity zone atop the 410-km discontinuity. Synthetic waveforms based on the IASP91 model (Kennett & Engdahl, 1991) are also shown in the shaded region (in blue, also see Figure S1 in Supporting Information S1). A reduced slowness of 11 s/° is applied to the time axis for illustration purposes. (b) Similar to (a) but for the P waves of event 20080604. Vertical arrows highlight the waveform mismatches possibly due to the potential lateral variations. (c) Similar to (a) but for the S waves of event 20080604 on the tangential component. A reduced slowness of 21 s/° is applied. Note that clear S waves are not recorded for the other event with a smaller magnitude.

et al., 2014). Using the differential travel times and amplitudes in the triplicated wave trains (e.g., Brudzinski & Chen, 2003; Grand & Helmberger, 1984; LeFevre & Helmberger, 1989) also has the advantage of isolating the anomaly near the turning points from the entire ray paths, because different triplicated phases share almost the same paths near the source and receivers but are separated at the turning points (penetration depths). Therefore, triplications are effective tools to constrain the seismic structure at the target region (e.g., from 300 to 450 km).

However, there are also tradeoffs between model parameters (Shearer, 2000), that is, different models yield very similar triplication waveforms. The most important tradeoff, which will influence our measurement of the low-velocity anomaly, is the one between the size of the low-velocity zone and the location of the 410-km discontinuity. For example, triplication observations are similar between models with a large wave-speed reduction with an uplifted 410-km discontinuity and a small low-velocity anomaly with a depressed interface, as demonstrated via a synthetic data set by Li, Chen, et al. (2022).

To investigate the influence of this important tradeoff, we varied the discontinuity depth from 380 to 440 km with an interval of 10 km. At each discontinuity depth, we performed a separate inversion. Results and discussions are based on the models from all these inversions.

2.2.2. 1D Inversion Scheme

We inverted both P-wave and S-wave triplication data using the FastTrip software (Li et al., 2021). FastTrip is an open-source waveform inversion package that is based on QSEIS (Wang, 1999) and the Niching Genetic

Algorithm (Koper et al., 1999) for the 1D forward modeling and model selection, respectively. In the forward modeling part, we aligned and stacked the first P-waveform at larger distances (i.e., 20–22°) to represent the P-wave source time function. For the S-wave, we convolved the P-wave source time function with a constant t^* value of 3 s to simulate the effect of attenuation of the S-waves (Stein & Wysession, 2009). We note that the choice of the source time function and the attenuation factor (i.e., t^*) will not affect the inversion results much because we focused more on the differential arrivals and amplitudes between the triplicated waveforms, rather than the individual pulses.

With FastTrip, we can achieve better waveform fittings for array data than the trial-and-error approach, reveal the tradeoffs between model parameters, and quantitatively estimate the uncertainties. With 100 CPUs, one inversion cycle (10,000 waveform simulations and model selections) with 13 unknown model parameters (i.e., two of them are immediately on the discontinuity to capture the velocity jump, and the others represent gradual velocity changes away from the interface) can be completed within hours.

3. Results

3.1. Waveform Fitting

The comparisons between the recorded (black) and synthetic (red) waveforms for the P waves on the vertical component for events 20090824 and 20080604 are respectively shown in Figures 2a and 2b. The S waves for event 20080604 on the tangential component are shown in Figure 2c. Synthetic waveforms for P and S waves are calculated using the average P- and S-wave speed models (i.e., the mean value of the models in Figures 3b and 3d, respectively). The synthetics correlate well with the data, with an average cross-coefficient higher than 0.9 and 0.8 for the P- and S-waves, respectively. Both the relative arrival time and amplitude between the triplicated phases are well-matched for most of the stations, indicating the reliability of the structures near the 410-km discontinuity.

Some mismatches exist between the synthetics and the data for the P waves (e.g., LN.FXI, HE.LOH, and BJ.MIY in Figure 2b). We attribute this to inconsistencies in the data, which may be caused by small-scale lateral heterogeneities. For example, the amplitude of the second pulse for station LN.FXI is small (∼20% of the first pulse). However, for nearby stations LN.SHS (at a larger distance) and LN.GAX (at a smaller distance), the amplitude for the second pulse is larger (∼50%). This phenomenon also occurs for the first pulse for stations HE.LOH and BJ.MIY, compared with their nearby stations. This type of mismatch and its possible reasons are systematically analyzed in the discussion section.

3.2. P-Wave Speed Models

For the P-wave data, we performed inversions at discontinuity depths from 380 to 440 km with an interval of 10 km. There are in total 14 inversions for two earthquakes. For each event, we first found the best-fitting model with the minimum misfit (L2 norm of waveform differences) and then defined the acceptable models (e.g., shaded regions in Figure 3) with misfits no larger than twice the minimum misfit of the best-fitting model.

For both events, there are no acceptable models when the discontinuity depth is either shallower than 390 km or deeper than 410 km, based on the waveform fits of the 1D inversion. At interface depths between 390 and 410 km, the first-order patterns of the preferred model sets for event 20080604 (i.e., the shaded red regions in Figures 3a–3c) are similar to that for event 20090824 (i.e., the shaded grey regions in Figures 3a–3c): a low-velocity anomaly is located above the discontinuity, whereas the velocity at shallow depths (above 310 km) is similar to the IASP91 model. This overall consistency between the models confirms the robustness of the derived P-wave model, despite subtle differences that may arise from slightly different earthquake locations.

For most of the inverted models, there is a low-velocity zone (with a smaller velocity gradient compared with the IAPS91 model) above the discontinuity. Importantly, the size of the low-velocity zone decreases as the depth of the discontinuity increases, which exhibits the tradeoffs between these two parameters. For example, when there is no uplift (Figure 3c), a less pronounced low-velocity anomaly is observed in the inverted models (i.e., data can be fitted without introducing a more significant low-velocity anomaly atop the 410-km discontinuity as in Figures 3a and 3b). However, there is a maximum P-wave reduction of 0.3 km/s when the 410-km discontinuity is uplifted by 20 km (Figure 3a). Therefore, it is crucial to consider this tradeoff between the discontinuity depth and the velocity above the discontinuity.
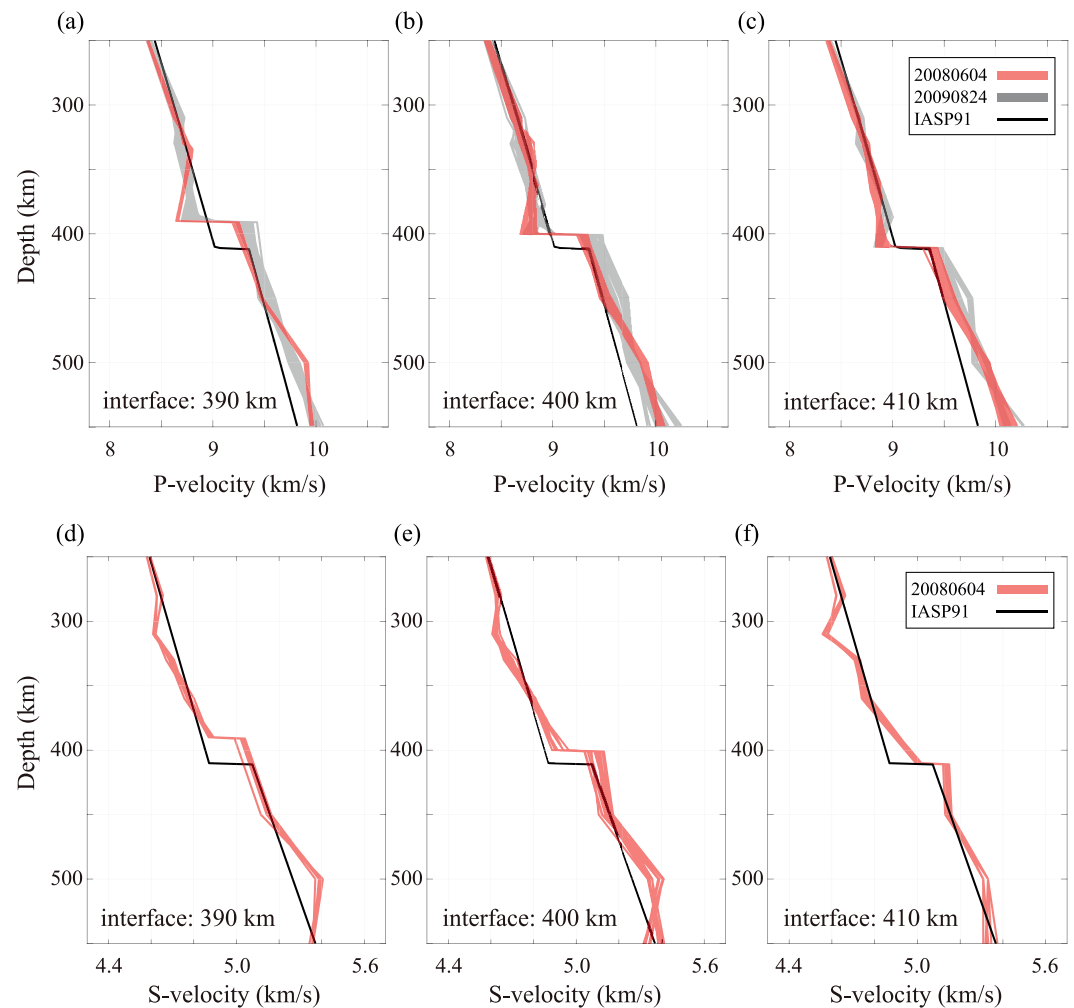
Figure 3. 1D-inversion results. (a) Inverted acceptable P-wave velocity models with a fixed discontinuity depth of 390 km. The model sets for events 20080604 and 20090824 are in shaded red and grey, respectively. The black curve represents the IASP91 model (Kennett & Engdahl, 1991). (b) Similar to (a) but for a discontinuity depth of 400 km. (c) Similar to (a) but for a discontinuity depth of 410 km. (d) Inverted acceptable S-wave velocity models from event 20080604 with a fixed discontinuity depth of 390 km. The black curve represents the IASP91 model. (e) Similar to (d) but for a discontinuity depth of 400 km. (f) Similar to (d) but for a discontinuity depth of 410 km.

3.3. S-Wave Models

For the S-wave inversions, the acceptable discontinuity depths are also from 390 to 410 km (Figures 3d–3f). Different from the P-wave profiles, the S-wave models exhibit no sign of a localized low-velocity anomaly atop the 410-km discontinuity (Figures 3d and 3e). In addition, there is another different feature in the S-wave models, that is, a prominent low-velocity anomaly between 300 and 370 km. The existence of this shallow anomaly is not much affected by the discontinuity depth.

We did not invert for the structures near the 660-km discontinuity since the other triplication generated from the 660-km discontinuity does not affect the waveforms we are interested in (i.e., in the shaded region, also see Figure S2 in Supporting Information S1).

4. Discussions

4.1. Quasi-2D Inversion

In the inverted models, one key difference between the P- and S-wave models is the location of low-velocity anomalies. The observed low-velocity anomaly in the P-wave models lies within about 30 km above the 410-km

discontinuity (note that the exact location of this interface may not locate at 410 km depth). In contrast, the most prominent anomaly in the S-wave models is centered about 60 km above the 410-km discontinuity.

However, since a 1D approximation is assumed, it must be clarified that the different features between the P- and S-wave results are not artifacts of the 1D assumption. This is because, given the complex 3D and 2D (i.e., in a certain cross-section) structure of the subducting slab (e.g., Takeuchi et al., 2014; Tao et al., 2018), the 1D assumption may not be a reasonable approximation. For example, Wang et al. (2014), through forward modeling, proved that 2D and 3D structures can affect triplication travel time and waveforms. This influence is enhanced when the ray paths are parallel to the strike direction of the slab (Wang et al., 2014). Although, in this study, the ray paths are perpendicular to the Wadati–Benioff zone where the 2D and 3D influence is less severe (e.g., Han et al., 2021; Wang et al., 2014), we propose a new quasi-2D inversion scheme to quantitatively consider the effects of lateral variations.

In this quasi-2D inversion, we treat the structures near the turning points (i.e., inside the dashed box in Figure 1b) still as the 1D case. However, outside of this inversion box where triplications have fewer constraints, we selected the tomographic model FWEA18 as the background model. During the inversion, we kept the values outside the box unchanged, and only modify the velocity profile inside the inversion box (e.g., the depth range is from 300 to 450 km).

On the one hand, this quasi-2D inversion included the 2D structures near the source (i.e., the subducting slab) and receiver. On the other hand, unlike a traditional 2D inversion, this quasi-2D inversion has fewer free parameters (i.e., 13 free parameters) given the 1D structure inside the inversion box.

Accordingly, for the forward modeling part, we have to replace the 1D simulation tool QSEIS (Wang, 1999) with a GPU-based 2D finite-difference method (Li et al., 2014). We prefer a GPU-based code because, with enough GPUs (e.g., 20 NVIDIA V100 cards), the inversion (with 10,000 simulations) can still be finished within one day.

For the P waves (Figures 4a and 4c), both the 1D synthetics (in red, Figure 4c) and quasi-2D synthetics (in blue, Figure 4c) generally match the recorded data. In addition, some waveform mismatches in the 1D synthetics (Figure 2b) can be significantly improved with the quasi-2D inversion scheme (e.g., LN.FXI, HE.LOH, and BJ.MIY in Figure 4c). This indicates that those apparent inconsistencies in the data (e.g., in Figures 2b and 4c) are likely caused by the lateral variations of the subsurface structures in the subduction zone, and thus cannot be considered with the 1D inversion setting (Figure 5).

We show in Figure 4a the difference between the inverted P-wave models (with a discontinuity depth of 390 km) for the 1D (in red) and quasi-2D (in blue) settings. The first-order patterns are still the same (i.e., the low-velocity anomaly is close to the discontinuity, without any other anomaly near ~310 km).

For the S waves, Figure 4d shows that the 1D (in red) and quasi-2D (in blue) settings provide comparable waveform fits. However, Figure 4b indicates that there are discrepancies for the inverted models from those two settings, that is, the 1D assumption overestimated the velocity reduction near 320 km. With the 2D correction, although the amplitude of the shallow anomaly is reduced by about 30%, it is still a prominent feature. In addition, compared with the 1D inversion results, this anomaly is more vertically extensive in the quasi-2D results, which is more consistent with the features in the FWEA18 model (Figure 1c). In both the 1D and quasi-2D cases, there is no significant low-velocity anomaly in the vicinity of the 410-km discontinuity.

Such discrepancies between the P- and S-wave models have also been observed in the regional tomography model FWEA18 (Figures 1b and 1c). Although the FWEA18 model has a relatively lower resolution than the 1D or quasi-2D models in this study, it is inferred from the 3D inversion and thus suggests that the features we evidenced are not artifacts of the 1D or quasi-2D approximation.

4.2. The Shallow Low-Velocity Zone

The mechanism behind the low-velocity zone can be deciphered by the comparison between the P- and S-wave models. At depths between 300 and 370 km, no significant low-velocity anomaly is observed in the P-wave models from either this study (i.e., only −0.4% on average; Figure 4a) or the FWEA18 model (i.e., about −1.0%; Figure 1b). However, the reduction of the S-wave velocity is about −1.7% (e.g., Figure 4b) in this study, and −1.5% in the FWEA18 model (Figure 1c), respectively. We note that the exact amplitude of the wave speed
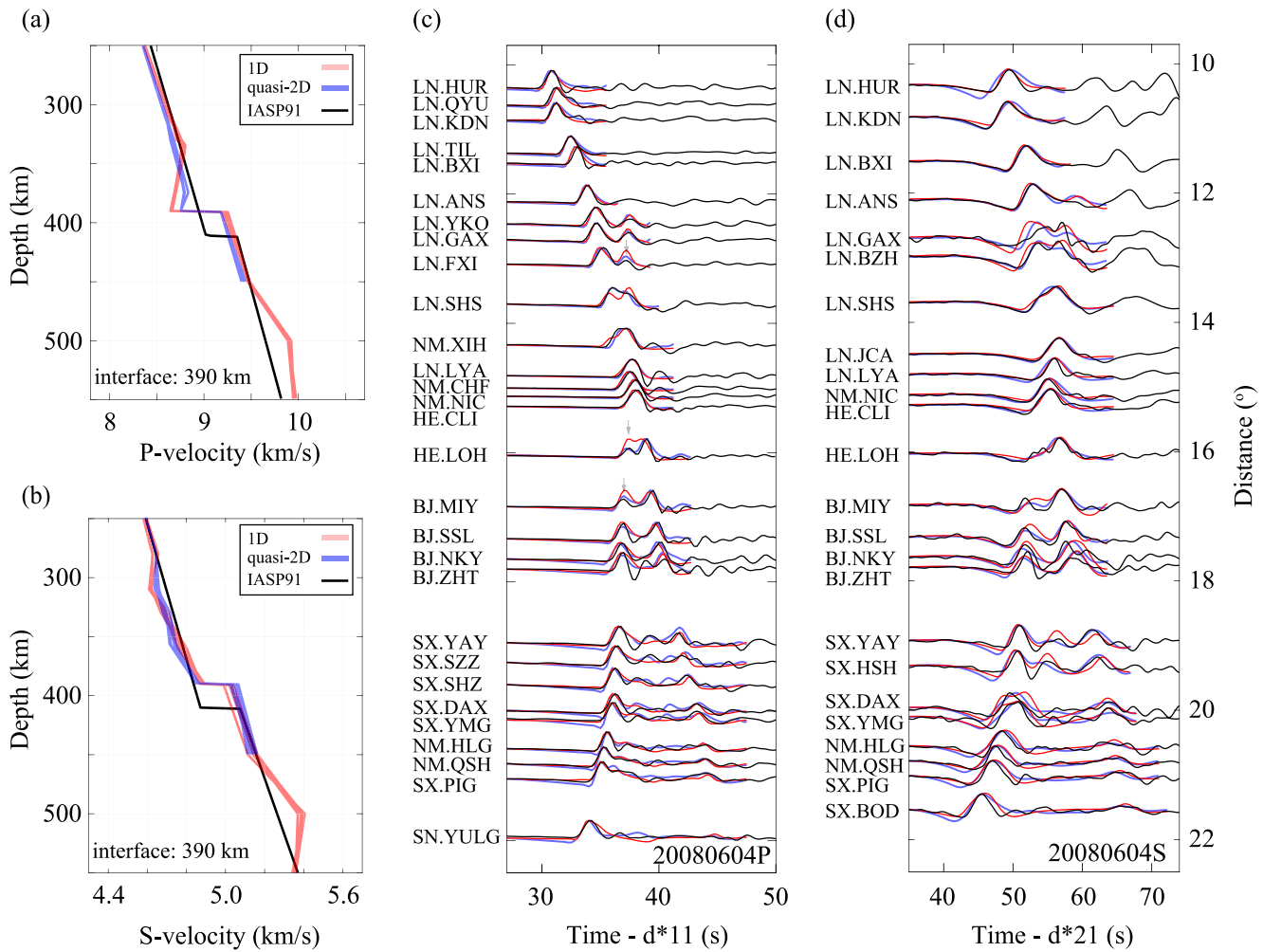
Figure 4. Quasi-2D inversion results and waveform comparisons. (a) Comparison of the P-wave models using the 1D inversion (shaded red) and quasi-2D inversion (shaded blue) for event 20080604 with an interface depth of 390 km. The black curve indicates the IASP91 model (Kennett & Engdahl, 1991). (b) Similar to (a), but for the S-wave models. (c) Waveform comparisons between the data (in black), 1-D synthetics (in red), and quasi-2D synthetics (in blue) for the P-waves of event 20090824 on the vertical component. The misfit window is denoted by the length of the synthetic waveforms. The vertical arrows mark the improvements in waveform fitting with the quasi-2D inversion scheme. (d) Similar to (c), but for the S-waves.

reduction depends on the reference model and the model parameterizations in the inversion, but the feature of a higher Vp-to-Vs ratio in this depth range is robust (e.g., compared to the IASP91 model between 300 and 370 km).

A high-temperature anomaly would decrease both the P- and S-wave speeds (e.g., −0.4 to −0.6 m/s/K and −0.3 to −0.4 m/s/K for the P- and S-wave speed reductions, respectively) as reported in several studies (Jackson et al., 2000; Kern, 1982; Sinogeikin et al., 1998). As this low-velocity anomaly more predominantly affects the S waves between 300 and 370 km, it cannot be caused by a thermal anomaly alone.

Hydrous phases, for example, water-saturated olivine with 0.4% water by weight, can only lower the S-wave speeds by a very small amount (e.g., less than 1% in Mao & Li, 2016). Therefore, the prominent low-velocity anomaly in the S-wave models is unlikely to be explained by hydrous phases alone.

However, partial melting can significantly lower the S-wave speeds. Melt-induced reduction in the S-wave speed is greater than that in the P-wave speed (Faul et al., 1994; Toomey et al., 1998). For example, with about 5% of melt, the reduction in the S-wave speed is twice larger than the reduction in the P-wave speed. Considering melt as a diffuse and thin grain-boundary film, it would reduce the S-wave speed by reducing the resistance to shear of grain boundaries, without significantly affecting the P-wave speed.

Moreover, recent electrical conductivity imaging (Li et al., 2020) in the same cross-section exhibits a low-resistivity (i.e., high-conductivity) column from the root of the Changbaishan volcano down to the 410-km discontinuity
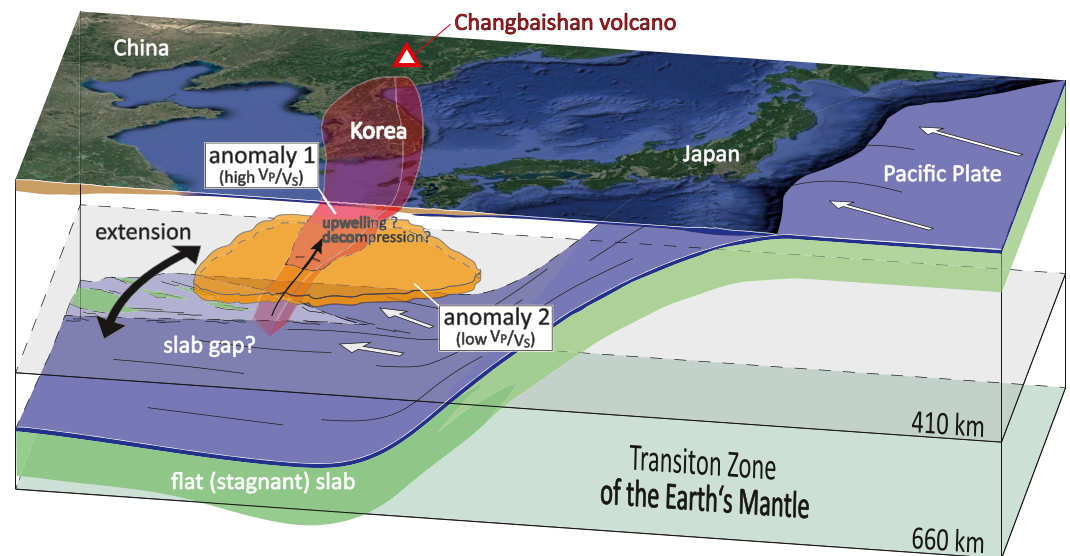
Figure 5. Sketch of the preferred interpretations, showing the seismic velocity anomalies beneath the Changbaishan volcano (red triangle). The subducting Pacific slab is shown in green (i.e., the harzburgitic layer) and purple (i.e., oceanic crust). The first low-velocity anomaly (with a high Vp/Vs ratio) is shown in red (modified from Figure 5 in Tang et al., 2014) and is attributed to partial melting, which could originate either from deep dehydration of the slab (Zhao et al., 2009) or from buoyant materials coming from the lower mantle via a possible gap in the slab (Tang et al., 2014). The second low-velocity anomaly is drawn in orange (with a low Vp/Vs ratio) and is likely caused by the reduction of the effective moduli during the phase transformation between olivine and wadsleyite (Durand et al., 2012).

(Figure 1d). A comparison between the seismic and conductivity images shows that this low-resistivity region is laterally offset by about 100 km to the west of the S-wave velocity anomaly in the upper mantle (Figure 1c). This discrepancy might be due to different sensitivities to partial melt distribution and temperature between seismic velocity and electric conductivity, and/or differences in measurement locations (e.g., Cordell et al., 2020). Nevertheless, the lateral offset diminishes with increasing depth and the bottom of the low-resistivity anomaly agrees with the location of the slab gap in the mantle transition zone from the seismic model (Figure 1c).

This is a strong evidence of partial melting because resistivity is very sensitive to interconnected conductive materials. However, it is challenging to further convert the velocity reduction to the amount of partial melt because there is a large uncertainty in the relationship between rock properties and seismic velocities (Wei & Shearer, 2017). For example, for the same S-wave speed reduction of 10%, Hier-Majumder and Tauzin (2017) and Yamauchi and Takei (2016) derived different melt estimations of 4% and 1%, respectively. Finally, the source of such partial melting can originate from either slab dehydration (Huang & Zhao, 2006) or from the buoyant materials coming from the lower mantle via the gap in the slab (Tang et al., 2014).

4.3. The Low-Velocity Zone Atop the 410-km Discontinuity

Both the P- and S-models in the FWEA18 model exhibit low-velocity anomalies atop the 410-km discontinuity (i.e., from 120°E to 132°E in Figures 1b and 1c). We note that the exact value of the velocity reduction inferred from our study can be affected by the choice of the reference model and model parameterizations. Nevertheless, since the model parameterizations are the same for both the P- and S-wave models, it is reasonable to compare the first-order patterns between them. P-wave models clearly illustrate a low-velocity anomaly atop the discontinuity regardless of the interface depth and inversion approach (i.e., 1D or quasi-2D), whereas there is no clear evidence for a low-velocity anomaly in the S-wave models atop the 410-km discontinuity.

Given the similar or even smaller amplitude of the S-wave anomaly compared to the P-wave anomaly in the FWEA18 model (Figures 1b and 1c), together with a lower Vp-to-Vs ratio (e.g., compared to the IASP91 model) in our velocity-depth profiles (i.e., a more prominent P-wave speed reduction), we propose that this anomaly cannot be caused by partial melting, since partial melting should cause more significant reductions in the S-wave speeds.

A relatively deeper mantle transition zone has been reported in the region (e.g., Sun et al., 2021), attributed to a higher temperature given the positive Clapeyron slope of the olivine-wadsleyite phase transition. Yet, despite this indirect evidence for a slightly warmer transition zone, temperature anomalies should affect both the P- and S-wave speeds to similar extents (e.g., Jackson et al., 2000; Kern, 1982; Sinogeikin et al., 1998). Therefore, thermal anomalies alone (if any) could not be responsible for the more pronounced P-wave speed reduction. We also note that our previous rejection of a deeper mantle transition zone (e.g., the interface depth is no deeper than 410 km) is based on the waveform fits of the 1D inversion. By utilizing the 2D inversion setting to improve the waveform fits, it is possible to accept a deeper discontinuity without contradicting the mantle transition zone depth reported by Sun et al. (2021).

Our result can be viewed as an "anchor point", that is, an average 1-D model with a vertical resolution of ~20 km (width of the Fresnel zone), of the FWEA18 model near the turning points of the ray paths (i.e., shown in Figure 1d, in black). In addition, we considered different discontinuity depths and found that all possible inter-face locations exhibit consistent conclusions. Thus, our results confirm that the features in the FWEA18 model in the vicinity of the 410-km discontinuity are not artifacts due to either the damping or the fixed discontinuity depth during the full-waveform inversion. We note that the FWEA18 model shows that this low-velocity anomaly extends to a wider horizontal scale (i.e., from 120°E to 132°E). Therefore, we propose that this localized low-velocity anomaly is likely caused by the reduction of the effective moduli during the phase transformation (Anderson, 1998; Jackson, 2007; also see Figure S3 in Supporting Information S1).

In zones where olivine (low-pressure phase) and wadsleyite (high-pressure phase) coexist (e.g., a thickness of 10 km for the 410-km discontinuity (Durand et al., 2012)), any pressure perturbation by a passing seismic wave (e.g., on the order of ~10^{-7} GPa) would disrupt the equilibrium and potentially induce the phase transformation in one way or the other (Li & Weidner, 2008). Durand et al. (2012) showed that this transformation loop does not affect S waves much, but potentially influences the P waves. This is consistent with the more prominent P-wave speed reduction in both the FWEA18 model and our study. In addition, since this mechanism is related to the phase transition, it would explain why the low-velocity anomaly is only limited to the region atop the 410-km discontinuity.

Elastic moduli are intrinsic properties of materials and can depend either on chemical variations, pressure, temperature, and grain size (e.g., Hilairet et al., 2007; Isaak, 1992; Wang et al., 2003). For sake of clarity and in order not to induce overinterpretation, we only deal with effective moduli in this study, which can for example, be reduced by grain size reduction.

5. Conclusions

The upper mantle beneath the Changbaishan volcano is characterized by two seismic low-velocity anomalies with distinct Vp-to-Vs ratios. These features cannot be explained by the same mechanism.

We selected two earthquakes and a sub-linear array to perform high-resolution 1D and quasi-2D inversions. Our derived velocity-depth profile can be viewed as a high-resolution "anchor point" in the cross-section of the full-waveform inversion model FWEA18 and confirms the distinct behaviors of the P and S waves in the FWEA18 model (Figures 1b and 1c). Complementary electrical conductivity imaging also exhibits a column of abnormally high conductivity from the 410-km discontinuity up to the root of the Changbaishan volcano.

Based on the above evidences, we argue that the two distinct low-velocity anomalies in the upper mantle are not due to the same mechanism. Near the 410-km discontinuity, the low-velocity anomaly would be caused by the reduction of the effective moduli during the phase transformation (e.g., Durand et al., 2012). However, the other low-velocity anomaly which mostly affects the S waves and the associated high electrical conductivity between 200 and 370 km are more likely caused by partial melting, which can originate either from slab dehydration (Huang & Zhao, 2006) or from buoyant materials via a tear in the Pacific slab (Tang et al., 2014).

Data Availability Statement

The software FastTrip used to perform the waveform inversion is freely accessible (https://github.com/liji-aqi0315/FastTrip, https://doi.org/10.5281/zenodo.6392194). Seismic stations used in this study are described in Zheng et al. (2010), https://doi.org/10.1785/0120090257, and the waveform data are freely accessible in the Zenodo repository (https://doi.org/10.5281/zenodo.7102579) (Li, Li, et al., 2022).

References

Anderson, D. L. (1998). The scales of mantle convection. *Tectonophysics*, *284*(1–2), 1–17. https://doi.org/10.1016/s0040-1951(97)00169-8

Bissig, F., Khan, A., & Giardini, D. (2022). Evidence for basalt enrichment in the mantle transition zone from inversion of triplicated P-and S-waveforms. *Earth and Planetary Science Letters*, *580*, 117387. https://doi.org/10.1016/j.epsl.2022.117387

Bozdag, E., Peter, D., Lefebvre, M., Komatitsch, D., Tromp, J., Hill, J., et al. (2016). Global adjoint tomography: First-generation model. *Geophysical Journal International*, *207*(3), 1739–1766. https://doi.org/10.1093/gji/ggw356

Brudzinski, M. R., & Chen, W. P. (2003). A petrologic anomaly accompanying outboard earthquakes beneath Fiji-Tonga: Corresponding evidence from broadband P and S waveforms. *Journal of Geophysical Research*, *108*, B6. https://doi.org/10.1029/2002jb002012

Chen, M., Niu, F., Liu, Q., Tromp, J., & Zheng, X. (2015). Multiparameter adjoint tomography of the crust and upper mantle beneath East Asia: 1. Model construction and comparisons. *Journal of Geophysical Research: Solid Earth*, *120*(3), 1762–1786. https://doi.org/10.1002/2014jb011638

Chen, Y., Zhang, Y., Graham, D., Su, S., & Deng, J. (2007). Geochemistry of Cenozoic basalts and mantle xenoliths in Northeast China. *Lithos*, *96*(1–2), 108–126. https://doi.org/10.1016/j.lithos.2006.09.015

Chen, Y. J., & Pei, S. (2010). Tomographic structure of East Asia: II. Stagnant slab above 660 km discontinuity and its geodynamic implications. *Earthquake Science*, *23*(6), 613–626. https://doi.org/10.1007/s11589-010-0760-4

Cordell, D., Unsworth, M. J., Lee, B., Díaz, D., Bennington, N. L., & Thurber, C. H. (2020). Integrating magnetotelluric and seismic images of silicic magma systems: A case study from the Laguna del Maule volcanic field, central Chile. *Journal of Geophysical Research: Solid Earth*, *125*(11), e2020JB020459. https://doi.org/10.1029/2020jb020459

Durand, S., Chambat, F., Matas, J., & Ricard, Y. (2012). Constraining the kinetics of mantle phase changes with seismic data. *Geophysical Journal International*, *189*(3), 1557–1564. https://doi.org/10.1111/j.1365-246x.2012.05417.x

Ekstrom, G., Nettles, M., & Dziewoński, A. M. (2012). The global CMT project 2004–2010: Centroid-moment tensors for 13,017 earthquakes. *Physics of the Earth and Planetary Interiors*, *200*, 1–9. https://doi.org/10.1016/j.pepi.2012.04.002

Faul, U. H., Toomey, D. R., & Waff, H. S. (1994). Intergranular basaltic melt is distributed in thin, elogated inclusions. *Geophysical Research Letters*, *21*(1), 29–32. https://doi.org/10.1029/93gl03051

Fichtner, A., Kennett, B. L., Igel, H., & Bunge, H. P. (2009). Full seismic waveform tomography for upper-mantle structure in the Australasian region using adjoint methods. *Geophysical Journal International*, *179*(3), 1703–1725. https://doi.org/10.1111/j.1365-246x.2009.04368.x

French, S. W., & Romanowicz, B. A. (2014). Whole-mantle radially anisotropic shear velocity structure from spectral-element waveform tomography. *Geophysical Journal International*, *199*(3), 1303–1327. https://doi.org/10.1093/gji/ggu334

Grand, S. P., & Helmberger, D. V. (1984). Upper mantle shear structure of North America. *Geophysical Journal International*, *76*(2), 399–438. https://doi.org/10.1111/j.1365-246x.1984.tb05053.x

Han, G., Li, J., Guo, G., Mooney, W. D., Karato, S. I., & Yuen, D. A. (2021). Pervasive low-velocity zone atop the 410-km discontinuity beneath the northwest Pacific subduction zone: Implications for rheology and geodynamics. *Earth and Planetary Science Letters*, *554*, 116642. https://doi.org/10.1016/j.epsl.2020.116642

Hayes, G. P., Moore, G. L., Portner, D. E., Hearne, M., Flamme, H., Furtney, M., & Smoczyk, G. M. (2018). Slab2, a comprehensive subduction zone geometry model. *Science*, *362*(6410), 58–61. https://doi.org/10.1126/science.aat4723

Hier-Majumder, S., & Tauzin, B. (2017). Pervasive upper mantle melting beneath the western US. *Earth and Planetary Science Letters*, *463*, 25–35. https://doi.org/10.1016/j.epsl.2016.12.041

Hilairet, N., Reynard, B., Wang, Y., Daniel, I., Merkel, S., Nishiyama, N., & Petitgirard, S. (2007). High-pressure creep of serpentine, interseismic deformation, and initiation of subduction. *Science*, *318*(5858), 1910–1913. https://doi.org/10.1126/science.1148494

Huang, J., & Zhao, D. (2006). High-resolution mantle tomography of China and surrounding regions. *Journal of Geophysical Research*, *111*(B9), B09305. https://doi.org/10.1029/2005jb004066

Isaak, D. G. (1992). High-temperature elasticity of iron-bearing olivines. *Journal of Geophysical Research*, *97*(B2), 1871–1885. https://doi.org/10.1029/91jb02675

Jackson, I. (2007). In G. Schubert (Ed.), *Treatise on geophysics* (Vol. 2, pp. 493–525).

Jackson, J. M., Sinogeikin, S. V., & Bass, J. D. (2000). Sound velocities and elastic properties of γ-Mg2SiO4 to 873 K by Brillouin spectroscopy. *American Mineralogist*, *85*(2), 296–303. https://doi.org/10.2138/am-2000-2-306

Kennett, B. L. N., & Engdahl, E. R. (1991). Traveltimes for global earthquake location and phase identification. *Geophysical Journal International*, *105*(2), 429–465. https://doi.org/10.1111/j.1365-246x.1991.tb06724.x

Kern, H. (1982). P-and S-wave velocities in crustal and mantle rocks under the simultaneous action of high confining pressure and high temperature and the effect of the rock microstructure.

Komatitsch, D., & Tromp, J. (1999). Introduction to the spectral element method for three-dimensional seismic wave propagation. *Geophysical Journal International*, *139*(3), 806–822. https://doi.org/10.1046/j.1365-246x.1999.00967.x

Koper, K. D., Wysession, M. E., & Wiens, D. A. (1999). Multimodal function optimization with a niching genetic algorithm: A seismological example. *Bulletin of the Seismological Society of America*, *89*(4), 978–988. https://doi.org/10.1785/bssa0890040978

Kuritani, T., Ohtani, E., & Kimura, J. I. (2011). Intensive hydration of the mantle transition zone beneath China caused by ancient slab stagnation. *Nature Geoscience*, *4*(10), 713–716. https://doi.org/10.1038/ngeo1250

LeFevre, L. V., & Helmberger, D. V. (1989). Upper mantle P velocity structure of the Canadian Shield. *Journal of Geophysical Research*, *94*(B12), 17749–17765. https://doi.org/10.1029/jb094ib12p17749

Lei, W., Ruan, Y., Bozdag, E., Peter, D., Lefebvre, M., Komatitsch, D., et al. (2020). Global adjoint tomography—Model GLAD-M25. *Geophysical Journal International*, *223*(1), 1–21. https://doi.org/10.1093/gji/ggaa253

Li, D., Helmberger, D., Clayton, R. W., & Sun, D. (2014). Global synthetic seismograms using a 2-D finite-difference method. *Geophysical Journal International*, *197*(2), 1166–1183. https://doi.org/10.1093/gji/ggu050

Li, J., Chen, M., Koper, K. D., Zhou, T., Xi, Z., Li, S., & Li, G. (2021). FastTrip: A fast MPI-accelerated 1D triplication waveform inversion package for constraining mantle transition zone discontinuities. *Seismological Society of America*, *92*(4), 2647–2656. https://doi.org/10.1785/0220200475

Li, J., Chen, M., Ning, J., Bao, T., Maguire, R., Flanagan, M. P., & Zhou, T. (2022). Constraining the 410-km discontinuity and slab structure in the Kuril subduction zone with triplication waveforms. *Geophysical Journal International*, *228*(2), 729–743. https://doi.org/10.1093/gji/ggab361

Li, L., & Weidner, D. J. (2008). Effect of phase transitions on compressional-wave velocities in the Earth's mantle. *Nature*, *454*(7207), 984–986. https://doi.org/10.1038/nature07230

Li, S., Li, J., Ferrand, T. P., Lv, M., Xi, Z., Maguire, R., et al. (2022). Deep geophysical anomalies beneath the Changbaishan Volcano [Dataset]. Zenodo. https://doi.org/10.5281/zenodo.7102579

Li, S., Weng, A., Li, J., Shan, X., Han, J., Tang, Y., et al. (2020). Deep origin of Cenozoic volcanoes in Northeast China revealed by 3-D electrical structure. *Science China Earth Sciences*, *63*(4), 533–547. https://doi.org/10.1007/s11430-018-9537-2

Mao, Z., & Li, X. (2016). Effect of hydration on the elasticity of mantle minerals and its geophysical implications. *Science China Earth Sciences*, *59*(5), 873–888. https://doi.org/10.1007/s11430-016-5277-9

Shearer, P. M. (2000). *Upper mantle seismic discontinuities* (Vol. 117, pp. 115–132). Geophysical Monograph-American Geophysical Union.

Sinogeikin, S. V., Katsura, T., & Bass, J. D. (1998). Sound velocities and elastic properties of Fe-bearing wadsleyite and ringwoodite. *Journal of Geophysical Research*, *103*(B9), 20819–20825. https://doi.org/10.1029/98jb01819

Stahler, S. C., Sigloch, K., & Nissen-Meyer, T. (2012). Triplicated P-wave measurements for waveform tomography of the mantle transition zone. *Solid Earth*, *3*(2), 339–354. https://doi.org/10.5194/se-3-339-2012

Stein, S., & Wysession, M. (2009). *An introduction to seismology, earthquakes, and Earth structure*. John Wiley & Sons.

Sun, Y., Hier-Majumder, S., Tauzin, B., Walter, M., Ballmer, M., Xu, Y., & Kim, S. (2021). Evidence of volatile-induced melting in the northeast Asian upper mantle. *Journal of Geophysical Research: Solid Earth*, *126*(10), e2021JB022167. https://doi.org/10.1029/2021JB022167

Takeuchi, N., Kawakatsu, H., Tanaka, S., Obayashi, M., Chen, Y. J., Ning, J., et al. (2014). Upper mantle tomography in the northwestern Pacific region using triplicated P waves. *Journal of Geophysical Research: Solid Earth*, *119*(10), 7667–7685. https://doi.org/10.1002/2014jb011161

Tang, Y., Obayashi, M., Niu, F., Grand, S. P., Chen, Y. J., Kawakatsu, H., et al. (2014). Changbaishan volcanism in northeast China linked to subduction-induced mantle upwelling. *Nature Geoscience*, *7*(6), 470–475. https://doi.org/10.1038/ngeo2166

Tao, K., Grand, S. P., & Niu, F. (2018). Seismic structure of the upper mantle beneath eastern Asia from full waveform seismic tomography. *Geochemistry, Geophysics, Geosystems*, *19*(8), 2732–2763. https://doi.org/10.1029/2018gc007460

Tape, C., Liu, Q., Maggi, A., & Tromp, J. (2009). Adjoint tomography of the southern California crust. *Science*, *325*(5943), 988–992. https://doi.org/10.1126/science.1175298

Tatsumi, Y., Maruyama, S., & Nohda, S. (1990). Mechanism of backarc opening in the Japan Sea: Role of asthenospheric injection. *Tectonophysics*, *181*(1–4), 299–306. https://doi.org/10.1016/0040-1951(90)90023-2

Toomey, D. R., Wilcock, W. S., Solomon, S. C., Hammond, W. C., & Orcutt, J. A. (1998). Mantle seismic structure beneath the MELT region of the East Pacific Rise from P and S wave tomography. *Science*, *280*(5367), 1224–1227. https://doi.org/10.1126/science.280.5367.1224

Tromp, J., Tape, C., & Liu, Q. (2005). Seismic tomography, adjoint methods, time reversal and banana-doughnut kernels. *Geophysical Journal International*, *160*(1), 195–216. https://doi.org/10.1111/j.1365-246x.2004.02453.x

Tseng, T. L., & Chen, W. P. (2008). Discordant contrasts of P-and S-wave speeds across the 660-km discontinuity beneath Tibet: A case for hydrous remnant of sub-continental lithosphere. *Earth and Planetary Science Letters*, *268*(3–4), 450–462. https://doi.org/10.1016/j.epsl.2008.01.038

Wang, G. F., Feng, X. Q., Yu, S. W., & Nan, C. W. (2003). Interface effects on effective elastic moduli of nanocrystalline materials. *Materials Science and Engineering: A*, *363*(1–2), 1–8. https://doi.org/10.1016/s0921-5093(03)00253-3

Wang, R. (1999). A simple orthonormalization method for stable and efficient computation of Green's functions. *Bulletin of the Seismological Society of America*, *89*(3), 733–741. https://doi.org/10.1785/bssa0890030733

Wang, T., Revenaugh, J., & Song, X. (2014). Two-dimensional/three-dimensional waveform modeling of subducting slab and transition zone beneath Northeast Asia. *Journal of Geophysical Research: Solid Earth*, *119*(6), 4766–4786. https://doi.org/10.1002/2014jb011058

Wei, S. S., & Shearer, P. M. (2017). A sporadic low-velocity layer atop the 410 km discontinuity beneath the Pacific Ocean. *Journal of Geophysical Research: Solid Earth*, *122*(7), 5144–5159. https://doi.org/10.1002/2017jb014100

Yamauchi, H., & Takei, Y. (2016). Polycrystal anelasticity at near-solidus temperatures. *Journal of Geophysical Research: Solid Earth*, *121*(11), 7790–7820. https://doi.org/10.1002/2016jb013316

Zhao, D., Tian, Y., Lei, J., Liu, L., & Zheng, S. (2009). Seismic image and origin of the Changbai intraplate volcano in East Asia: Role of big mantle wedge above the stagnant Pacific slab. *Physics of the Earth and Planetary Interiors*, *173*(3–4), 197–206. https://doi.org/10.1016/j.pepi.2008.11.009

Zheng, X. F., Yao, Z. X., Liang, J. H., & Zheng, J. (2010). The role played and opportunities provided by IGP DMC of China National Seismic Network in Wenchuan earthquake disaster relief and researches. *Bulletin of the Seismological Society of America*, *100*(5B), 2866–2872. https://doi.org/10.1785/0120090257

Zhu, H., Bozdag, E., & Tromp, J. (2015). Seismic structure of the European upper mantle based on adjoint tomography. *Geophysical Journal International*, *201*(1), 18–52. https://doi.org/10.1093/gji/ggu492

Zou, H., Fan, Q., & Yao, Y. (2008). U–Th systematics of dispersed young volcanoes in NE China: Asthenosphere upwelling caused by piling up and upward thickening of stagnant Pacific slab. *Chemical Geology*, *255*(1–2), 134–142. https://doi.org/10.1016/j.chemgeo.2008.06.022